Supplementary Materials

Pore interconnectivity as a design principle for durable high-voltage carbon-based supercapacitors

Carlos Maria Alava Limpo[1,#], Jong Hak Lee[2,3,#], Yong Kang Ong[3], Lucas M. Sassi[3], Yifan Rao[1,4], Lu Shi[1], Eng Tuan Poh[3], Keiji Tsuchiya[5], Daichi Takahashi[5], Barbaros Özyilmaz[1,2,3,4]

[1]Department of Material Science & Engineering, National University of Singapore, Singapore 117574, Singapore.

[2]Center for Advanced 2D Materials (CA2DM), National University of Singapore, Singapore 117546, Singapore.

[3]Department of Physics, National University of Singapore, Singapore 117551, Singapore.

[4]Institute for Functional Intelligent Materials (I-FIM), National University of Singapore, Singapore 117544, Singapore.

[5]Youth Engineering Co. Ltd, Niihama 792-0003, Japan.

[#]These authors contributed equally to this work.

Correspondence to: Prof. Barbaros Özyilmaz, Department of Materials Science and Engineering, National University of Singapore, 7 Engineering Drive 1, 117574, Singapore. E-mail: barbaros@nus.edu.sg

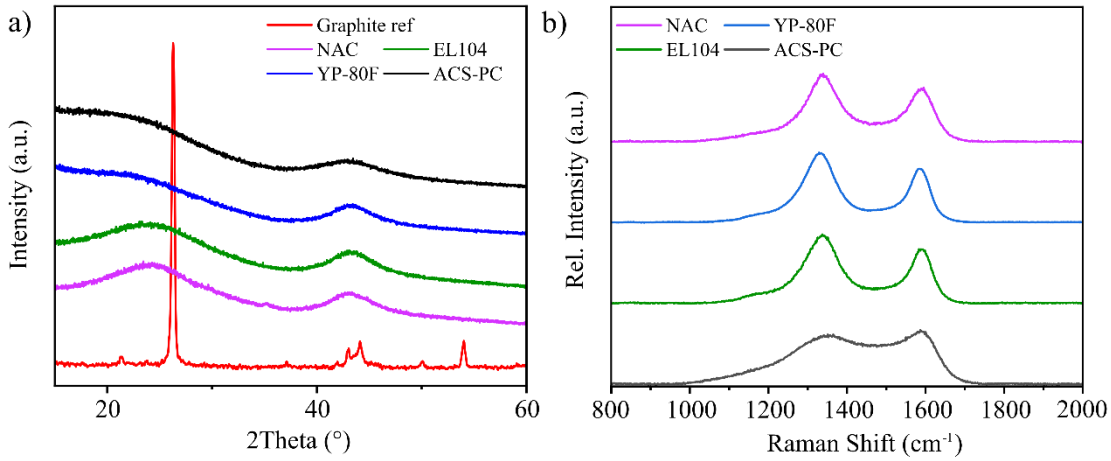

Supplementary Figure 1. Qualifying the degree of structural disorder in porous

carbons. (a) XRD Spectra of ACS-PC, EL104, YP-80F and NAC in comparison to a graphite reference.[1] All carbons exhibited broad peaks at 24 °, which is indicative of limited long-range graphitic ordering; (b) Raman Spectra of ACS-PC, EL104, YP-80F and NAC. All four carbons, especially ACS-PC exhibited broad D-peaks (~1330 cm^{-1}) and broad G-peaks (1580 cm^{-1}), indicating the presence of defect-rich sp^2 carbon, which contributes to their structural disorder.

Supplementary Table 1. Specifications of fabricated electrodes.

	Gurvich Pore volume of powder (cc/g)	**Electrode coating thickness (μm)**	**Mass Loading (mg/cm^2)**
ACS-PC	0.90	85	5.2
EL104	0.79	76	4.7
YP-80F	1.21	81	3.5
NAC	0.98	85	4.3

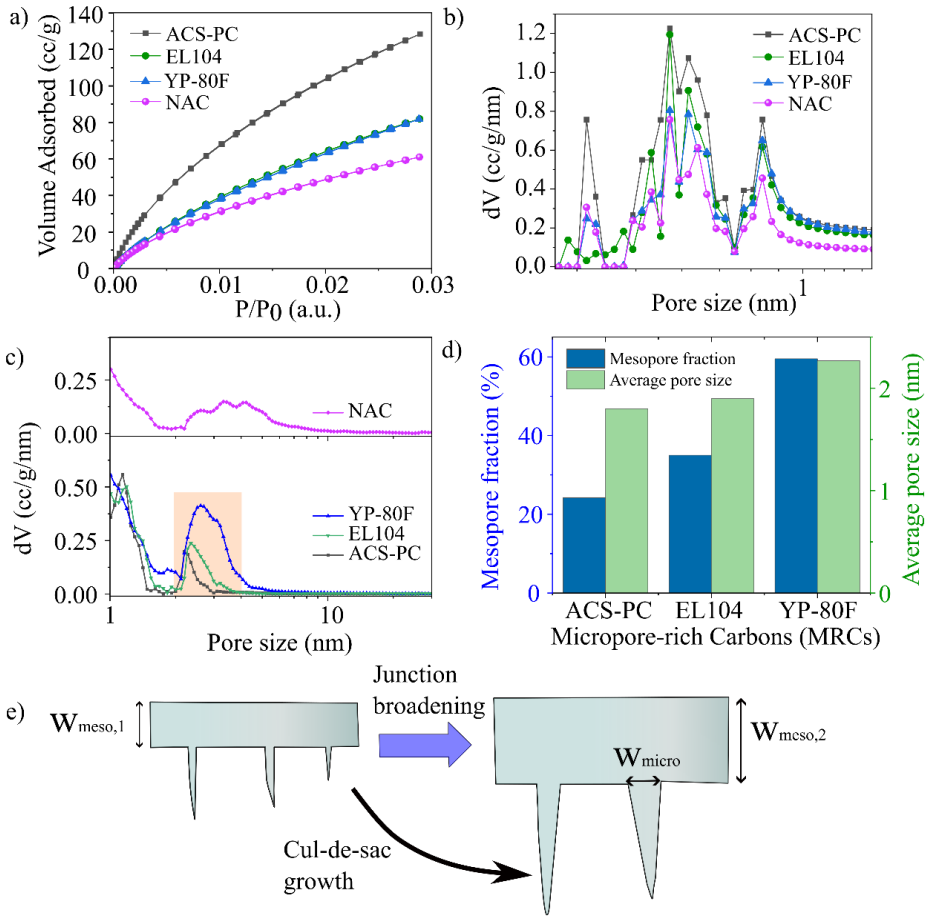

Supplementary Figure 2. Further investigation of pore size distributions within nanoporous carbons via CO_2 physisorption measurements and DFT analyses. (a) CO_2 physisorption isotherms of the four carbons. The steep uptake at low pressures revealed the presence of ultra-micropores (<1 nm); (b) Pore size distributions of micropores obtained via NLDFT for CO_2 physisorption. ACS-PC had the most abundant population of ultramicropores, which is consistent with its steep CO_2 uptake curve; (c) Pore size distribution curves obtained via Quenched Solids Density Functional Theory (QSDFT, adsorption kernel). Across the three commercial carbons, the population of pores between 2-4 nm in size was the most prominent difference. In contrast, NAC featured less micropores than the commercial carbons and a broader pore size distribution of mesopores ranging mostly below 10 nm in size; (d) Mesopore fraction and average pore size comparison of commercial carbons: ACS-PC, EL104 and YP-80F. As these three carbons exhibited Type I(b) isotherm features,[2] their pore size distributions suggest that the variation of their pore structures is focused on the enlargement of a mesoporous channel that acts as a main junction before splitting into micropore regions; (e) Assisting schematic of Supplementary Figure 2d, to visualize the effects of using activation methods. A combination of physical and chemical activations may be used to develop a carbon's porosity,[3] either through the expansion of existing pores (here noted as "junction broadening"), or via the propagation of existing pores to develop deeper microporous channels.

Supplementary Table 2. A comparative summary of the porosities of the four carbons

	Average pore size (nm)	**Gurvich pore volume (cc/g)**	**BET surface area (m^2/g)**	**Micropore surface area (< 0.42 nm) (m^2/g)**	**Ion-accessible surface area (%)**
ACS-PC	1.76	0.90	2000	218	89
YP-80F	2.27	1.21	2140	131	92
EL104	1.90	0.79	1680	99	95

NAC	3.00	0.98	1300	114	91

Gurvich pore volume was calculated relative to the volume of adsorbate adsorbed at the maximum relative pressure of the scan ($P/P_0 \sim 1.0$). For micropore metrics, the cumulative surface area up to 0.42 nm was used. This is because 0.42 nm corresponds to the characteristic bare ion size of the cation in this study (SBP^+) and therefore serves as a lower boundary for the smallest pore that can accommodate ion sorption. Even after accounting for the size constraint, a significant fraction of the surface area remains accessible for ion sorption. This motivates further investigation of their electrochemical performance as porous carbon electrodes.

Quantifying structure dependent pore occlusion from electrode fabrication process

Electrodes were fabricated by mixing carbon powder, CMC dispersant and PP (polypropylene) binder in a weight ratio of 90:4:6 and mixed in DI water to form an aqueous slurry. The resulting slurry was then made into an electrode, dried and sent for physisorption analyses. Upon noting down the BET surface area of the electrode, this value was then normalized against the carbon weight fraction (90%) to reflect the BET surface area of the sole porous component of the electrode. This was then subtracted by the initial BET surface area of the porous carbon prior to electrode fabrication, to elucidate a 'lost BET surface area' that may be attributed to the occlusion caused by binder intrusion within the pore structure (Equation S1).[4] Using a similar framework, a 'loss of pore volume' was also obtained (Equation S2).

$$Loss_{BET\ Surface\ Area} = Surface\ area_{BET} - \frac{Surface\ area_{BET}}{90\%} \qquad \text{(Equation S1)}$$

$$Loss_{Pore\ vol.} = Pore\ Volume - \frac{Pore\ Volume}{90\%} \qquad \text{(Equation S2)}$$

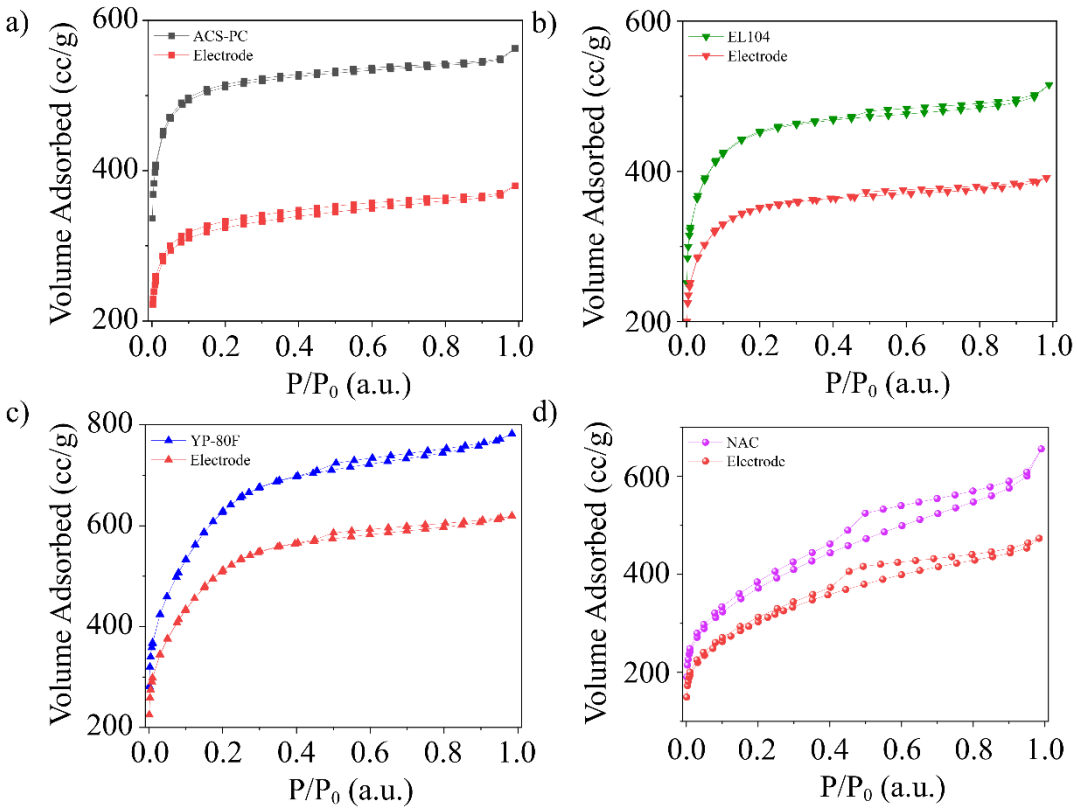

Supplementary Figure 3. Physisorption isotherm comparisons reveal pore blocking in micropore dominant carbons. ACS-PC, the most micropore-dominant carbon, exhibited the largest decrease in adsorbed N_2 at low P/P_0, suggesting that the population of detectable micropores decreased significantly after the slurry fabrication process. Intriguingly, the isotherm of ACS-PC's electrode showed a growth in low pressure hysteresis, whereby the volume differential between the adsorption and desorption slope increased from 3 cc/g to 12 cc/g after the slurry process. Developments in low-pressure hysteresis can be attributed to further inhibited kinetics within extremely narrow pore channels.[2] **(a)-(d)** Isotherm comparisons of powder and electrode equivalent of ACS-PC, EL104, YP-80F and NAC respectively.

Supplementary Table 3. Quantitative ranking of interconnectivity based on a carbon's susceptibility to surface area loss

	Surface area loss after binder incorporation (m^2/g)	**Interconnectivity ranking (1-highest)**
ACS-PC	630	4
EL104	470	3
YP-80F	220	2

NAC	130	1

During the electrode fabrication process, the incorporation of binders with the carbon slurry can cause pore-blocking,[4] To quantitatively rank the interconnectivity of these pore structures, we considered that poorly interconnected structures would lack the alternative pathways that can maintain access to sorption sites. This leaves poorly interconnected structures vulnerable to pore occlusion if blocking species intrude into its structure, causing significant losses of accessible surface area. Therefore, as an operational proxy, the interconnectivity of the carbons can be ranked based on the surface area loss of the carbon upon incorporating the same amount of binder.

Electrochemical evaluation of carbon electrodes

Supplementary Tables 4-7 present the capacitance retention trends of representative cells for each carbon. Although the tables clarify the capacitance at specific points in time, the degradation trajectory observed in **Figure 2b** is the focus.

Supplementary Table 4. Capacitance retention trends of ACS-PC

Float time (hours)	Capacitance (F/g) Cell-1	Capacitance (F/g) Cell-2	Capacitance (F/g) Cell-3
0	119.65	119.65	115.25
10	83.36	90.46	84.92

Supplementary Table 5. Capacitance retention trends of EL104

Float time (hours)	Capacitance (F/g) Cell-1	Capacitance (F/g) Cell-2	Capacitance (F/g) Cell-3
0	86.95	85.44	87.86
10	81.07	77.43	82.60
20	77.86	73.65	78.67
30	75.31	70.65	73.88
40	69.72	64.83	69.00

Supplementary Table 6. Capacitance retention trends of YP-80F

Float time (hours)	**Capacitance (F/g) Cell-1**	**Capacitance (F/g) Cell-2**	**Capacitance (F/g) Cell-3**
0	108.12	109.05	108.75
10	99.51	101.75	101.04
20	97.40	100.08	98.74
30	95.53	98.38	97.18
40	93.52	96.98	95.14
50	91.63	95.68	93.48
60	89.34	91.88	90.44
70	85.22	89.28	87.94

Supplementary Table 7. Capacitance retention trends of NAC

Float time (hours)	Capacitance (F/g) Cell-1	Capacitance (F/g) Cell-2	Capacitance (F/g) Cell-3
0	105.84	105.20	103.72
10	103.21	101.81	102.64
20	100.58	101.08	101.56
30	99.18	99.59	99.95
40	97.78	100.62	98.34
50	96.97	100.08	96.96
60	96.15	100.51	95.58
70	95.06	99.90	94.80
80	93.97	99.78	94.03
90	92.62	99.24	93.30
100	91.26	98.35	92.58
110	90.50	96.46	91.48
120	89.73	94.22	90.39
130	85.13	90.57	87.85
140	80.53	84.67	85.31

Supplementary Table 8. Preliminary electrochemical evaluation of porous carbons within their first 10 hours of testing

	BET Surface Area of electrode (m^2/g)	Capacitance @ 1A/g under 3V (F/g)	Capacitance after 10 hours of testing (F/g)	Surface Area Utilization (mF/m^2_{BET})
ACS-PC	1230	118	86 (73%)	96
EL104	1090	86	80 (93%)	79
YP-80F	1730	107	101 (95%)	62
NAC	1050	105	103 (97%)	100

Despite exhibiting the lowest surface area by a considerable margin, NAC exhibited comparable capacitance with YP-80F, which had a significantly higher surface area. To best visualize this discrepancy, the gravimetric capacitance of each carbon was divided by their characteristic BET surface area, to denote the degree of surface area utilization. This metric serves to quantitatively compare how effectively a porous scaffold can accommodate ion sorption for energy storage. This was motivated by how high surface area materials may contain ultramicropores that are too small for ions to access,[5] leading to inaccessible regions and underutilized surface area.

Nyquist Plot Analysis via Equivalent Circuit Fitting

To elucidate the ion transport characteristics among the different carbon samples, electrochemical impedance spectroscopy (EIS) was conducted to obtain Nyquist plots. At high frequencies, ions cannot respond to the rapidly alternating field. Hence the impedance response at this stage corresponds to frequency-independent series resistances (denoted $R_{independent}$). As the frequency decreases from 100 kHz to 1 kHz during the impedance measurement, ion motion is gradually enabled, and the associated resistance becomes observable in the impedance response as a depressed semicircle region. This feature can then be modelled by a parallel circuit consisting of a resistor (denoted R_{access}) and a constant phase element (CPE), where the latter captures the non-ideal response of the distributed pore interface.[6] R_{access} can be determined by measuring the real-axis span made by the semicircle feature, and can be used to quantify the resistance ions experience in infiltrating the porous carbon network.

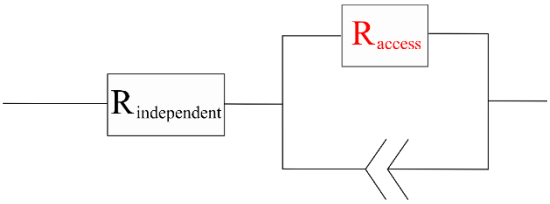

Supplementary Figure 4. Equivalent circuit model for fitting the high frequency semicircle. At this frequency range (100 kHz – 1 kHz), the semicircle region can be ascribed to the resistance encountered by ions accessing the pore network. This semicircle region is modelled by a resistor and Constant Phase Element (CPE) in parallel and will be denoted R_{access}.

Supplementary Table 9. Preliminary Impedance characterization of porous carbons before accelerated stress tests

	ESR @ 1kHz (Ohm)	R_{access} (Ohm)	$\chi^2/\|Z\|^2$ (a.u.)	Micropore Volume Fraction (a.u.)
ACS-PC	1.33	0.435	0.001	0.76
EL104	0.96	0.370	0.002	0.66
YP-80F	0.98	0.241	0.001	0.40
NAC	0.80	0.169	0.001	0.29

R_{access} is obtained through the length that the high-frequency semicircle covers along the x-axis. We observed that R_{access} decreased with decreasing micropore fraction. Given that the electrolyte was standardized across the samples as 1.5 M SBPBF4 in propylene carbonate, R_{access} is associated with the aspect of ion-transport resistance that is network-architecture dependent. The quality of the fitting is represented in the column titled '$\chi^2/|Z|^2$'. All values are low, indicating good fitting.

Post-mortem Raman Spectra comparison

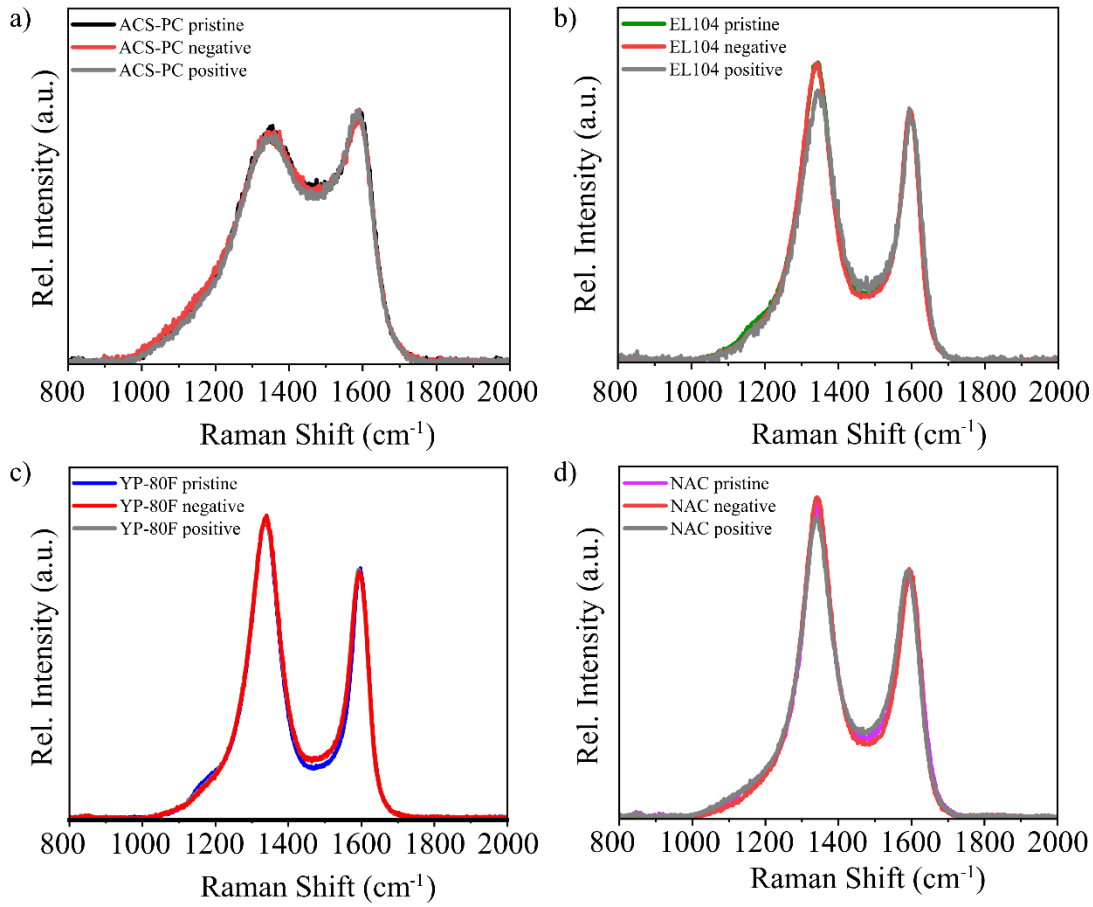

Supplementary Figure 5. Raman spectra comparison of pristine electrodes against their aged counterparts. Across all carbons, aged electrodes were extracted upon reaching End-of-Life. In all four carbons, the spectra of the electrodes exhibited no drastic changes upon aging. This suggests that the short-range sp^2 carbon framework did not undergo significant transformations upon electrochemical stress.

Post-mortem SEM analysis

Once coin cells had incurred a 20% capacitance loss from the electrochemical stress tests, electrode pairs were extracted, rinsed and washed in propylene carbonate before being vacuum-dried overnight at 70 °C. SEM images were extracted to assess morphology changes, because the degradation of propylene carbonate is reported to form passivation layers on electrode surfaces.[7] However, in this study, no pronounced morphological differences were observed across all carbons upon reaching End-of-Life (Supplementary Figures 6-9). For Figures S6-S9, scale bars in all images were set to represent 10 μm.

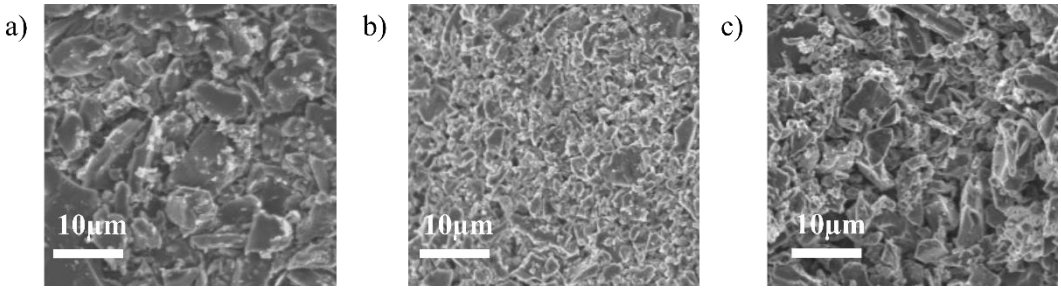

Supplementary Figure 6. ACS-PC electrodes a) Pristine state, before tests. b) Aged positive electrode. c) Aged negative electrode.

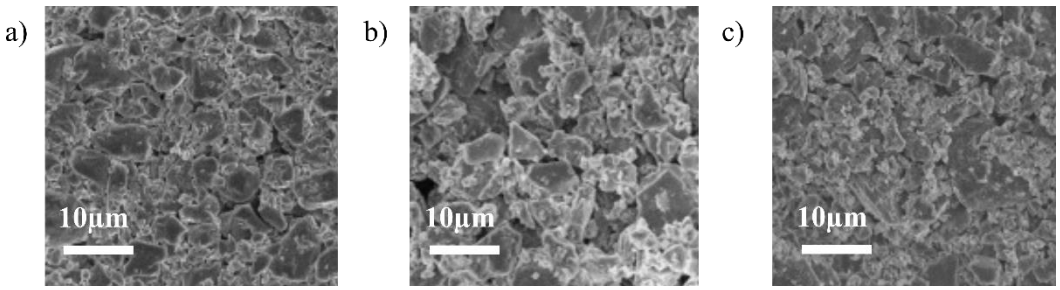

Supplementary Figure 7. EL104 electrodes a) Pristine state, before tests. b) Aged positive electrode. c) Aged negative electrode.

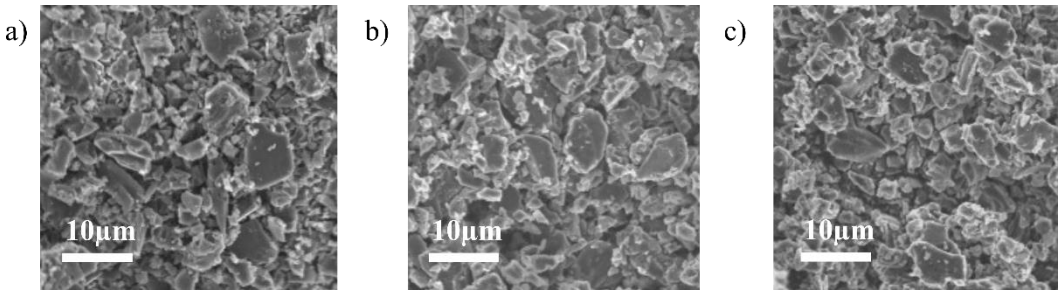

Supplementary Figure 8. YP-80F electrodes a) Pristine state, before tests. b) Aged positive electrode. c) Aged negative electrode.

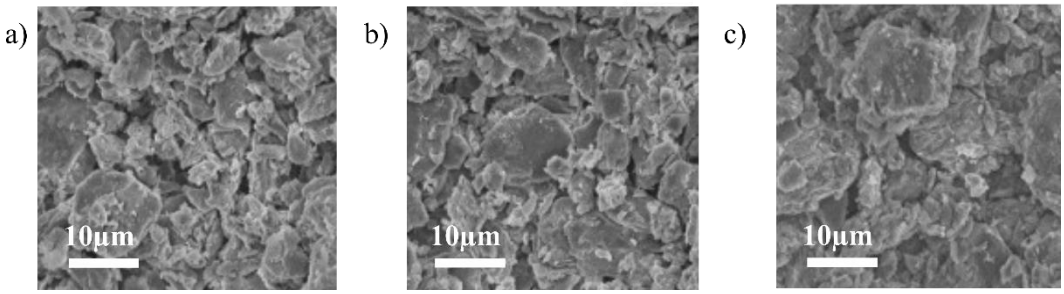

Supplementary Figure 9. NAC electrodes a) Pristine state, before tests. b) Aged positive electrode. c) Aged negative electrode.

Surface Area analysis comparison of aged NAC and YP-80F electrodes

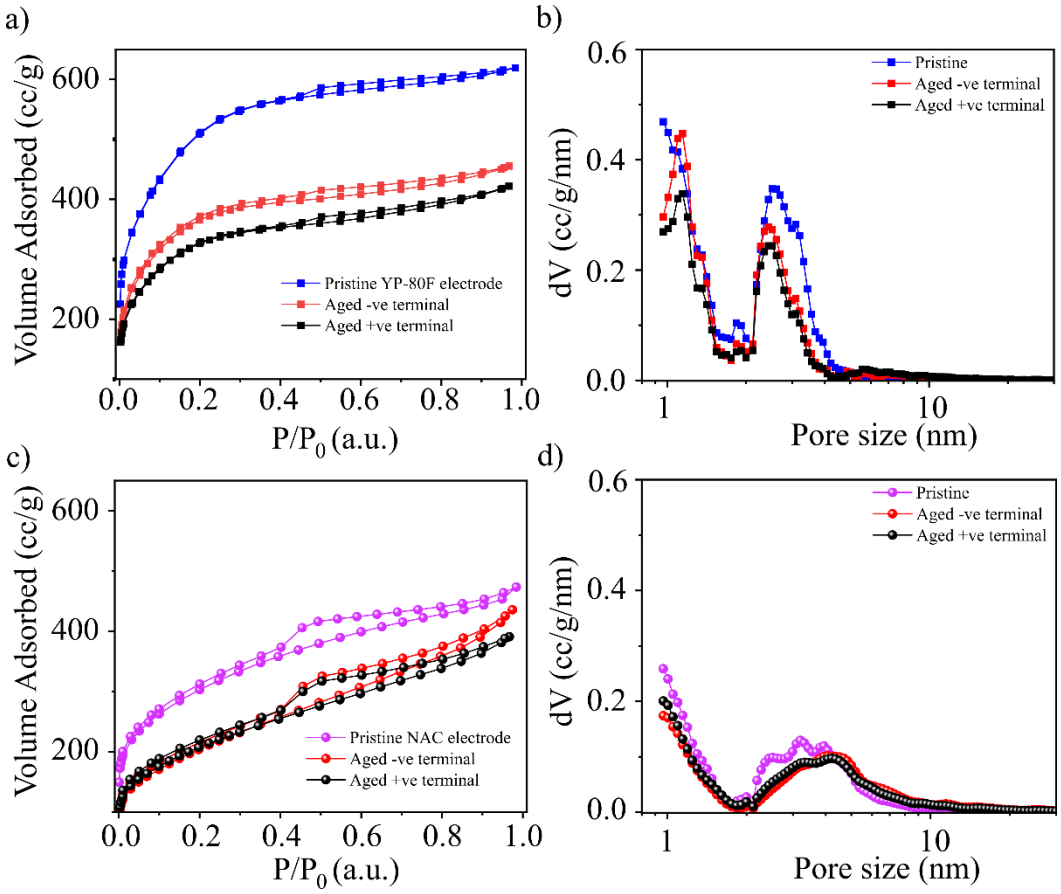

Supplementary Figure 10. Further investigation of aged electrode pore structures of YP-80F and NAC, taken at a 70-hour mark. Post-mortem physisorption analysis of YP-80F a) N_2 adsorption-desorption isotherm comparison of pristine electrode and aged electrodes. b) Pore size distribution comparison obtained via QSDFT. Post-mortem physisorption analysis was also performed on NAC electrodes. c) Isotherm comparison of aged NAC electrodes against pristine counterparts. d) Pore size distribution comparison obtained via QSDFT. Although YP-80F and NAC exhibited similar mesoporosity, their capacitance retention trends diverged more prominently nearing the 70-hour mark. These observations are counter-intuitive to YP-80F's significantly higher surface area and therefore necessitated a pore structure comparison at the same time state of 70 hours. Evidently, YP-80F's isotherms showed a significant reduction of total nitrogen uptake, suggesting reduced pore accessibility after cycling. QSDFT measurements further suggest that there was a notable reduction of micropores and mesopores in YP-80F, evident in the prominent peak decrease upon aging. In contrast, NAC's overall nitrogen uptake has a much lower reduction upon

cycling for the same duration. Moreover, changes in NAC's pore size distribution were significantly mitigated.

Demonstrating cycling stability in an alternate sulfone-based electrolyte system

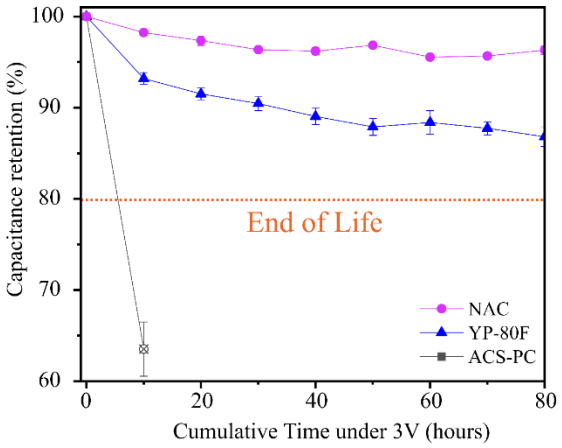

Supplementary Figure 11. Capacitance retention curves obtained for coin cells made with the Sulfone electrolyte. The specific sulfone-based electrolyte used was KKE-20MSX (Japan Carlit Co. Ltd, Japan), comprising of 59 wt.% Sulfolane, 7 wt.% Diethyl Sulfone, 34 wt.% $SBPBF_4$. Enhanced capacitance retention was observed for YP-80F and NAC upon switching to the sulfone-based electrolyte. Still, NAC exhibited significantly mitigated capacitance loss than YP-80F, which is consistent with the trends observed for the propylene carbonate system. In contrast, ACS-PC failed to show enhanced capacitance retention even after switching to the sulfone-based electrolyte.

REFERENCES

1. Lee J.H; Loh N.D.; Yeo Z.Y.; et al. Engineering a Hierarchy of Disorder: A New Route to Synthesize High-Performance 3D Nanoporous All-Carbon Materials, Adv Mater. **2024**, 36, 2402628 https://doi.org/10.1002/adma.202402628

2. Thommes M.; Kaneko K.; Neimark A.V.; et al. Physisorption of gases, with special reference to the evaluation of surface area and pore size distribution (IUPAC Technical Report), Pure Appl. Chem. **2015**, 87, 1051-1069. https://doi.org/10.1515/pac-2014-1117

3. Li L.; Sun F.; Gao J.; Wang L; Pi X.; Zhao G. Broadening the pore size of coal-based activated carbon via a washing-free chem-physical activation method for high-

capacity dye adsorption, RSC Adv. **2018**, 8, 14488-14499 https://doi.org/10.1039/c8ra02127a

4. Im J.; Liu X.; O'Keefe C.A.; Grey C.P.; Forse AC. Pore-intrusion of Polymeric Binder in Supercapacitor Electrodes Decreases Capacitance. Nanoscale, **2026**, 18(22), 11880-11889. https://doi.org/10.1039/d5nr05282c

5. Nair M.R.; Chandran A.S.; Shukla N.; Prajapati V.K.; Roy T. Impact of Ion Geometry and Electrode Pore Interconnectivity on Charge Storage and Dynamics in Confined Nanopores. Advanced Theory and Simulations. **2026**, 9(2), e02219 https://doi.org/10.1002/adts.202502219

6. Lazanas A. Ch.; Prodromidis M.I. Electrochemical Impedance Spectroscopy - A Tutorial. ACS Measurement Science Au. **2023**, 3(3),162-193. https://doi.org/10.1021/acsmeasuresciau.2c00070

7. Ishimoto S.; Asakawa Y.; M. Shinya M.; Naoi K. Degradation Responses of Activated-Carbon-Based EDLCs for Higher Voltage Operation and Their Factors. J. Electroch. Soc. **2009**, 156, A563. https://doi.org/10.1149/1.3126423